Journal of Environmental Chemical Engineering 10 (2022) 107866

Contents lists available at ScienceDirect

Journal of Environmental Chemical Engineering

journal homepage: www.elsevier.com/locate/jece

Photodegradation of ibuprofen using CeO_2 nanostructured materials: Reaction kinetics, modeling, and thermodynamics

Noemi Gallucci [a,b], Maryam Hmoudah [a,c], Eugenie Martinez [d], Amjad El-Qanni [c], Martino Di Serio [a], Luigi Paduano [a,b], Giuseppe Vitiello [b,e,*], Vincenzo Russo [a,f,*]

[a] University of Naples Federico II, Department of Chemical Sciences, IT-80126 Naples, Italy
[b] CSGI, Center for Colloid and Surface Science, IT-50019 Sesto Fiorentino, FI, Italy
[c] An-Najah National University, Department of Chemical Engineering, Nablus, Palestine
[d] University of Grenoble Alpes, CEA, LETI, F-38000 Grenoble, France
[e] University of Naples Federico II, Department of Chemical, Materials and Production Engineering, IT-80125 Naples, Italy
[f] Åbo Akademi, Laboratory of Industrial Chemistry and Reaction Engineering, FI-20500 Turku/Åbo, Finland

ARTICLE INFO

Editor: Dr. G. Palmisano

Keywords:
Ibuprofen
CeO_2 nanoparticles
Photodegradation
Kinetic modeling
Thermodynamics

ABSTRACT

Ibuprofen is one the most used non-steroidal anti-inflammatory drug, which is considered an emerging pollutant that may contaminate surface and underground water. Photodegradation using nanomaterials is one of the most sustainable and cheap technologies that can be used in water purification. In this study, the photodegradation efficiency of in-house prepared ceria (CeO_2) nanostructured materials towards ibuprofen was assessed under UV irradiation. CeO_2 nanoparticles (NPs) were prepared through wet-chemical synthesis and characterized by several techniques. The photodegradation activity of the synthesized CeO_2-NPs was compared to the commercial Aeroxide TiO_2-P25. Small crystalline CeO_2-NPs were obtained with about 15 nm particle size, band-gap of 3.1 eV with irregular morphology. The surface area of CeO_2-NPs was estimated to be 76 ± 5 m^2/g. Dynamic light scattering analysis revealed that these nanoparticles have a strong tendency to self-aggregate and to form clusters in aqueous suspension. The results showed a slightly better performance of Aeroxide TiO_2-P25 compared to CeO_2-NPs. On the other hand, five reusability tests confirmed the stability of CeO_2-NPs in the reaction conditions, without any significant effect on their photodegradation activity. The goodness of the kinetic modeling of the experimental data was proven through the estimated kinetic parameters, together with the statistical information. The temperature effect confirmed that the higher the temperature, the greater the dissociation rate. Thus, there is a direct relationship between temperature, reaction rate, and the activation energy for each reaction. Furthermore, the thermodynamic parameters, namely: changes in Gibbs free energy (ΔG°), enthalpy (ΔH°), and entropy (ΔS°) have been reported revealing the efficient photodegradation performance of CeO_2-NPs.

1. Introduction

Pharmaceutical compounds, such as ibuprofen, have recently received a lot of attention due to their detection in water (surface and wastewater) and sediments [1]. Ibuprofen is considered one of the emerging pollutants that may contaminate surface and underground water due to the improper practices and disposal of unused medicine [2]. The presence of this compound in water bodies is considered problematic as many living beings can be adversely impacted due to the uncontrolled accumulation of these materials in the lipid tissues [3]. Numerous published studies and reviews about the occurrence, toxicity, and impact of ibuprofen were undertaken over the last few decades [4–7]. On the one hand, this material is resistant to conventional treatment methods such as sedimentation, coagulation, filtration, and biological processes [3,8]. On the other hand, most existing advanced wastewater treatment options, such as distillation, membrane filtration, and electrochemical treatment, are prohibitively expensive and face many operational challenges [9–11]. Therefore, photodegradation using nanomaterials is considered one of the sustainable state technologies that can be used in water purification [12–15]. This technology has many advantages because of the economic, environmentally friendly,

Abbreviations: 1-OH, 1-OH ibuprofen; 1-OXO, 1-OXO ibuprofen; CALC, Calculated; CI 95%, Confidence intervals calculated at 95%; EXP, Experimental; IBU, Ibuprofen; M, Correlation matrix.

* Correspondene to: University of Naples Federico II, Italy.
E-mail addresses: giuseppe.vitiello@unina.it (G. Vitiello), v.russo@unina.it (V. Russo).

https://doi.org/10.1016/j.jece.2022.107866
Received 8 March 2022; Received in revised form 20 April 2022; Accepted 4 May 2022
Available online 6 May 2022

Nomenclature

Abs	Absorbance [AU]
c_i	Concentration of component i [mol/m^3]
Ea_j	Activation energy for reaction j [kJ/mol]
F_{obj}	Objective function [–]
h	Plank constant [m^2 kg/s]
K_B	Boltzmann's constant [m^2 kg/s^2 K]
$k_{ref,j}$	Kinetic constant calculated at a reference temperature [(m^3/mol)(m^3/kg^n)s^{-1}]
n	Linearization coefficient for catalyst bulk density [–]
N_{data}	Number of available experimental data [–]
Q_{air}	Air volumetric flowrate [m^3/s]
r_j	Reaction rate of step j [mol/(kg s)]
r_{obs}	Observed reaction rate [mol/(m^3 s)]
R	Ideal gas constant [kJ/(K mol)]
t	Time [s]
T	Temperature [K]
T_{ref}	Reference temperature, 303 K [K]

Greek symbols

ΔG°	Gibbs free energy change [J/mol]
ΔH°	Enthalpy change [J/mol]
ΔS°	Entropy change [J/(mol K)]
v	Stirring rate [rpm]
ρ_B	Catalyst bulk density [kg/m^3]
ρ_{H2O}	Water density [kg/m^3]
υ_{ij}	Stoichiometric coefficient of component i in reaction j [–]

simple, and easily operated designs needed to eliminate contaminants of emerging concern from water [16]. This in turn improve drinking water quality and the safe reuse of water, thus protecting the environment, improving human health, and achieving sustainability goals [17].

Recently, cerium oxide has gained increasing attention for the degradation of organic contaminants in water [18–22]. In particular, a great interest has aroused the nanoparticles of cerium oxide nanoparticles (CeO_2-NPs) because of their reactivity, reusability, cost-effectiveness, and environmental impact [23]. Based on the literature survey presented in Table 1, most of the published works on the application of CeO_2-NPs solely in photodegradation focused on dyes, mainly on methylene blue. Therefore, paying attention to the photodegradation of emerging pollutants such as ibuprofen using CeO_2-NPs is important in the field of water purification. It should be mentioned that the uniqueness of these nanoparticles lies in the simplicity of conversion between Ce^{3+} and Ce^{4+}, the presence of defects, and the increase of the surface-to-volume ratio to CeO_2 in bulk [24–26]. Furthermore, the market price of Ce is around 4.57–4.71 $/kg compared to 11.1–11.7 $/kg for Ti [27], which oxides are nowadays considered the most efficient photocatalysts [28–30]. Thus, the use of CeO_2 could lead to a lower price of the catalyst.

In addition, CeO_2 is an n-type semiconductor with a band-gap at 3.1 eV [31,32], this wide band-gap of CeO_2 requires the use of UV light to activate the mechanism. To shift the band gap from 3.1 to 2.452.90 eV and, consequently, use visible light for photocatalytic activity, it is necessary to increase the number of defects in CeO_2-NPs [33]. The photocatalytic activity of CeO_2 is closely related to particle size, textural properties, and surface structure [34]. Therefore, an important parameter is the ratio Ce^{3+}/Ce^{4+}, which varies with the size of NPs that influence the photocatalytic activity. As Ce^{3+} switches to Ce^{4+} states, it results in high oxygen mobility in the CeO_2 lattice and in turn leads to a strong catalytic potential that happens without any structural modification of the fluorite lattice [33,35]. The change in energy can cause a surface effect on catalyst [24]. Another important parameter that determines the photocatalytic activity is the presence of oxygen vacancies in the CeO_2 lattice, as the oxygen vacancies vary, consequently, the properties of NPs vary [19,21,33,36].

In this paper, the synthesized CeO_2-NPs have been tested under

Table 1
Some previous published works on the photocatalytic activity of CeO_2 nanoparticles in photodegradation.

Synthesis	Pollutant (s)	Radiation	Highlights	Ref.
Co-precipitation method	Naphthol Blue Black dye	Sunlight	• CeO_2 has a low activity for the degradation of naphthol blue black dye. Doping with Mn showed increased photocatalytic activity.	[22]
An electron beam accelerator was used to modify pristine CeO_2	4-nitrophenol and methylene blue	Visible light	• EB can effectively narrow the band gap of metal oxides for the enhanced visible light photocatalytic activities.	[33]
Solvothermal method	Phenol and its derivatives (2-chlorophenol, 2-bromophenol and 2-nitrophenol)	Sunlight	• The interaction of UV photons induced defects at the surface of CeO_2.	[21]
Precipitation method	Methyl orange and methylene blue	UV-light	• CeO_2 nanoparticles showed a moderate degradation rate compared to other metal oxide-based nanoparticles.	[20]
Green synthesis using leaf extract of *Azadirachta indica* plant	Rhodamine B dye	UV-light	• Excellent photocatalytic activity of green CeO_2 nanoparticles towards RhB dye.	[37]
Hydrothermal method	Isopropyl alcohol	Visible light	• Confeito-like CeO_2 exhibits excellent performance for the decomposition of isopropyl alcohol to acetone. • Ce^{3+} induced oxygen vacancies in the lattice of CeO_{2-x}, and this resulted in an improvement in the activity.	[19]
Wet chemical method	Congo red and methyl orange	Visible light	• CeO_2 nanocubes showed high reactivity and stability for the photodegradation of dyes	[38]
Sonochemical-assisted method	Methylene blue	UV-light	• After 75 min of radiation, 85% of methylene blue were degraded.	[18]
Hydrothermal method	Methylene blue	In the dark, sunlight, and UV irradiation	• The performance varied based on the surface areas, nanoparticles shape and the content of oxygen vacancies.	[39]
Solution combustion technique	Methylene blue	UV-light	• The photocatalytic performance was optimized in terms of solution pH, catalyst dose, initial methylene blue, and UV irradiation time.	[40]
Commercial CeO_2 nanoparticles	Tropaeolin O	UV-light	• The effects of particle size and pH were investigated. • The degradation of Tropaeolin O was confirmed by toxicity experiments in the presence of CeO_2 NPs and marine crustaceans as A. salina.	[41]

ultraviolet (UV) irradiation for the photodegradation of ibuprofen. The performance of these NPs was compared with Aeroxide TiO_2-P25. Special attention was paid to the effect of air flow rate, stirring rate, temperature, catalyst bulk density, and initial concentration of the ibuprofen solution on the photodegradation efficiency of CeO_2-NPs. Reusability, kinetics modeling, activation energy, and thermodynamics parameterswere also addressed in this study.

2. Materials and methods

2.1. Materials

Ibuprofen solutions were prepared using 4-isobutyl-α-methylphenylacetic acid at 99% (Alfa Aesar). Cerium (III) nitrate hexahydrate salt ($Ce(NO_3)_3{\cdot}6H_2O$, purity > 99.999%), ammonia solution 30 v/v%, and hydrogen peroxide were purchased from Sigma-Aldrich (Milan, Italy). Milli-Q bidistilled water, also filtered using 0.20 μm filters, was obtained from Merck Millipore (Darmstadt, Germany). Commercial Aeroxide TiO_2-P25 was supplied by Evonik Industries (Essen, Germany) for comparative purposes in this study. All materials were used without any further treatment.

2.2. Methods

2.2.1. Synthesis of CeO_2 nanoparticles

Typically, CeO_2-NPs were prepared through a wet-chemistry synthesis in solvothermal conditions, according to reference [42]. First, 30 mL of an aqueous solution (0.5 M) of $Ce(NO_3)_3{\cdot}6H_2O$ salt was prepared and left under magnetic stirring for 10 min to induce a complete salt dissolution. Subsequently, 117 μL of hydrogen peroxide was added to the Ce(III) salt solution which was stirred for 5 min to favor the oxidation of Ce^{3+} to Ce^{4+}. A specific volume (~ 6 mL) of a diluted ammonia solution (7 M) was then added to this mixture to a pH of 8.8 to start the precipitation reaction. Afterward, the mixture was continuously stirred at 80 °C for 1 h to complete the reaction. After an hour, a yellow precipitate constituted by $Ce(OH)_4$ was obtained and washed three times with bidistilled Milli-Q water by centrifugation at 9000 rpm for 10 min. The pH was adjusted to pH 10 by using the ammonia solution and 30 mL of washed precipitate were treated at 120 °C for 24 h within a mini-reactor. The final CeO_2-NPs were repeatedly washed with bidistilled Milli-Q water by centrifugation at 9000 rpm for 10 min.

2.2.2. Physicochemical characterization

2.2.2.1. X-Ray diffraction (XRD) analysis. XRD measurements were performed with a PANalytical diffractometer (Malvern, Worcestershire, United Kingdom) with a nickel filter and CuKα radiation, with a step size of 0.02° and a counting time of 80 s per step, to investigate the formation and properties of CeO_2 crystalline phases. The average crystal size (τ) was evaluated using the Scherrer formula:

$$\tau = \frac{K\lambda}{\beta cos\theta} \quad (1)$$

where τ is the mean size of the crystallite domains, K is a dimensionless shape factor, λ is the X-ray wavelength, β is the broadening at half the maximum intensity (FWHM), θ is the Bragg angle.

2.2.2.2. X-ray photoelectron spectroscopy (XPS). Surface properties of CeO_2-NPs were investigated by XPS analyses which were carried out using a spectrometer VersaProbe II with a monochromatic Al Kν X-ray source ($h\nu$ = 1486,6 eV), a spot of 200 μm, and a dual-beam system (Ar^+ et $\bar{e}$) for charge compensation. The pass energy was set at 23.5 eV, leading to an overall energy resolution of 0.6 eV. Photoelectrons were collected at a take-off angle of 45°, which means a sampling depth of approximately 5 nm. The relative atomic composition (% at.) is given with an uncertainty of ± 20% using tabulated relative sensitivity factors. Decomposition of the spectra was done using Voigt functions after Shirley's background subtraction with the Multipak software.

2.2.2.3. Transmission electron microscope (TEM). Morphological properties of CeO_2-NPs were investigated by TEM. The analyzed sample was prepared by placing 10 μL of nanoparticle suspension on one side of a 200 mesh carbon-coated copper grid that was allowed to dry in air. TEM images were obtained using a FEI TECNAI G2 200 kV microscope (ThermoFisher Scientific, Waltham, USA) equipped with a high-angle annular dark-field (HAADF) detector for high-resolution imaging.

2.2.2.4. Dynamic light scattering (DLS). DLS measurements were performed to measure the size of CeO_2-NPs in an aqueous environment with a home-made instrument composed of a Photocor compact goniometer (Moscow, Russia), SMD 6000 Laser Quantum 50 mW light source (Laser Quantum, Fremont, CA, USA) operating at 532.5 Å, a photomultiplier (PMT-120-OP/B) and a correlator (Flex02-01D) from Correlator.com (Shenzhen, China). The experiments were carried out on 1 mL of an aqueous suspension of CeO_2-NPs at the constant temperature (25.0 ± 0.1) °C, by using a thermostatic bath and at the scattering angle θ of 90°. The scattered intensity correlation function was analyzed using a regularization algorithm. The diffusion coefficient of each population of particles was calculated as the z-average of the diffusion coefficients of corresponding distributions. These DLS measurements have been carried out in triplicate with the aim to verify the reproducibility. Specifically, each measurement was constituted by 12 scans of 60 s to determine the mean hydrodynamic radius and its error.

2.2.2.5. Surface area and porosimeter analysis. Specific surface area (S_{BET}) and the pore volume (V_P) of CeO_2-NPs were evaluated by generating seven-point isotherms at 77 K for N_2 adsorption (Autosorb-1, Quantachrome) using a particular amount of the sample capable of providing a specific surface area equal to 5 m^2 in the sample cell. The mesopore volume (V_{BJH}), the mean pore radius (r_P), and the pore size distributions were estimated by the Barrett–Joyner–Halenda (BJH) method applied to the desorption branch of the isotherm [43].

2.2.2.6. Ultra-violet and visible light diffuse reflection (UV–vis DRS) spectroscopy. UV-Vis DRS measurements on powdered CeO_2-NPs were carried out using a UV-2600i UV–VIS spectrophotometer, 230 V (Shimadzu, Milan, Italy), equipped with an integrating sphere ISR-2600Plus operating in a wavelength range of 220–1400 nm. Barium sulfate was exploited as a reflectance standard. The measured intensity was expressed as the value of the Kubelka–Munk function F(R), while the band-gap value was evaluated by linearization of the plot of $(F(R)h\nu)^{1/2}$ against $h\nu$.

2.2.2.7. High-pressure liquid chromatography (HPLC). Ibuprofen concentration analyses were carried out using an Agilent 1100 High Pressure Liquid Chromatography (HPLC) system, with a 70% w/w methanol, 30% w/w water mobile phase. The column used was a Phenomenex Luna C18, with a 5 μm particle size, 100 Å pore size, 250 mm length, and 4.6 mm internal diameter. The detector used was a diode array detector (DAD), with a 1024-element photodiode array, deuterium and tungsten lamps with a 190–950 nm. The software used for apparatus control and data collection was Agilent Chemstation. This system acquires the absorbance of the eluates in mAU (Absorbance Units) as a function of elution time in the whole emission interval of the lamps and outputs a 3D chromatogram with X elution time, Y wavelength, and Z signal intensity.

2.2.3. Photodegradation experimental set-up

Photodegradation experiments were conducted in a 1.5 L jacketed glass vessel, equipped with a three-neck head. The reactor was

connected to an ultra-thermostat to regulate the temperature at the desired level. The liquid temperature was monitored with a dedicated thermocouple. Air was fed to the reactor system using a digital flow-meter regulator (supplied by Bronkhorst), connected to a sintered filter used as a gas sparger, to provide a good gas-liquid interface in the mass transfer of air to the liquid phase. A coaxial 4 W UV lamp was mounted at the center of the reactor (Toshiba FL4BLB), characterized by a wavelength of $\lambda = 365$ nm, with dimensions of 15 cm × 1.5 cm. The liquid was stirred by a magnetic impeller at the desired rate.

In the classical execution of the experiment, the ibuprofen solution was prepared with the desired concentration and then loaded into the reactor and stirred at the set value. The reactor was closed with the lid and connected to the thermostat, set at a pre-specified reaction temperature. The airflow was adjusted with a pressure reducer to 1 bar and the digital flow meter was set at a fixed flow. At this point, the catalyst was loaded into the reactor. The reactor was then shielded before the UV lamp to reduce any ray dispersion, avoiding any risk to the operator. A first sample was collected to measure the concentration of ibuprofen (time = 0 sample). The reaction was then started by switching on the lamp, withdrawing samples periodically to follow the reaction kinetics until a maximum time of 5 h. Each sample was then centrifuged at 3300 rpm for 30 min, and the resulting liquid sample was analyzed by UV–VIS spectroscopy (UV-Vis Jasco V-550). A classical spectrum was reported in the Supplementary material (Fig. S.1). A calibration curve was built at $\lambda = 222$ nm, where ibuprofen absorption reached the maximum value, obtaining the calibration curve reported in Eq. (2), valid in a concentration range between 0.0 and 0.05 mol/m^3 (Fig. S.2).

$$c_{IBU} = (0.113 \pm 0.001)Abs,\ R^2 = 0.99 \quad (2)$$

Where *Abs* represents the absorbance and c_{IBU} is the ibuprofen concentration expressed in mol/m^3.

To investigate the reaction kinetics, together with eventual mass transfer limitations, several experiments were conducted by varying the operational conditions in a wide range. The summary of the adopted reaction conditions is reported in Table S.1.

2.2.4. Modeling and parameter estimation

Matlab R2020b was used to perform all the modeling activities reported in the present work. Ordinary differential equations were solved using the *ode23s* routine, while parameter estimation activity was performed with the *particleswarm* algorithm. The objective function was calculated as follows [34]:

$$F_{obj} = \frac{1}{N_{data}} \sqrt{\sum_{i=1}^{N_{data}} \left(\frac{c_{i,EXP} - c_{i,CALC}}{c_{i,EXP}} \right)^2} \quad (3)$$

The confidence intervals were calculated using the *nlparci* algorithm.

3. Results and discussion

3.1. Physico-chemical features of synthesized CeO_2 nanoparticles

Characterization of CeO_2 NPs was carried out using XRD and XPS measurements. The XRD pattern of CeO_2-NPs, shown in Fig. 1, indicated the presence of the typical peaks of a face-centered cubic (FCC) structure (JCPDS no. 81-0792) [34,44,45]. The peaks obtained at the diffraction angles (2θ) of 29°, 33°, 47°, 56°, and 59° correspond to the Miller indices (hkl) indicating the crystalline planes (111), (200), (220), (311) and (222) respectively, as shown in Fig. 1, and confirming the formation of CeO_2 nanoparticles with a fluorite-type crystalline structure. The mean crystallite sizes estimated from Scherrer's formula were close to 18 ± 1 nm.

Then XPS analysis was performed to obtain information on the chemical composition of the surface of the CeO_2 nanoparticles. The survey spectrum is plotted in Fig. 2A, showing the main characteristic

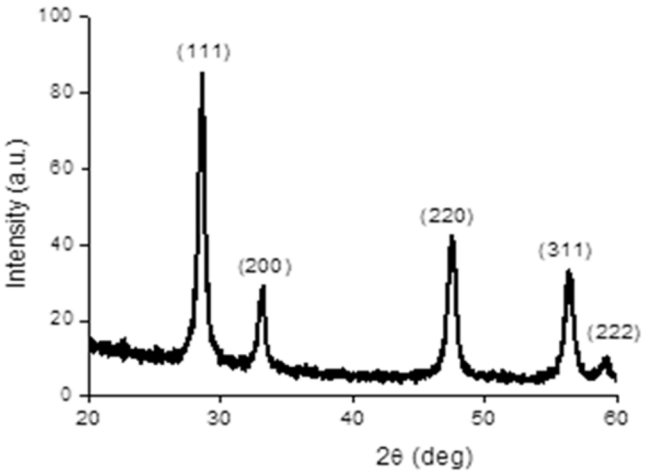

Fig. 1. XRD pattern of CeO_2 NPs.

peaks of CeO_2 (Ce 3*d*, Ce 4*d* and O 1*s*) as well as carbon contamination (C 1*s*). A zoom on the oxygen O1*s* core level is presented in the inset, highlighting two contributions related to O-Ce bonds from the CeO_2 NPs and O—C bonds from hydrocarbon surface contamination. The spectrum of the Ce3*d* core level is reported in Fig. 2B. This spectrum exhibits strong satellite features (cf^{1}L) to the main peaks (cf^0). For each component of the Ce $3d_{5/2}$ - Ce $3d_{3/2}$ doublet, 5 peaks were used to fit all these contributions, each of them being assigned to one of the Ce oxidation states (Ce^{3+} and Ce^{4+}) as indicated in Table S.2. The Ce^{3+}/Ce^{4+} ratio was estimated to be equal to 0.4, as deduced from the areas of these different components.

Morphological and textural features of CeO_2-NPs were analyzed by TEM (Fig. 3A). A representative TEM image shows the formation of small nanoparticles of about 15 nm in size and with irregular morphology. At the same time, it suggests a strong tendency of these nanoparticles to self-aggregate, forming clusters with a size comparable to that obtained by DLS analysis (Fig. 3B). As observed from the hydrodynamic radius distribution, the main population is centered at about 530 ± 70 nm confirming a fast and significant self-aggregation of bare CeO_2 nanoparticles when they were in an aqueous suspension. In addition, S_{BET} of CeO_2-NPs was measured by N_2 adsorption at 77 K and the estimated surface area was equal to 76 ± 5 m^2/g. The adsorption/desorption isotherm shows a type IV-hysteresis, which is typical of porous materials (see Fig. S.3). Size distribution of pores was estimated according to the BJH model based on the desorption branch of the isotherm, indicating that the total volume of the pores is equal to 0.22 cm^3/g, while the pore distribution (as derivative of the pore volume to the radius) shows the presence of a single population of pores with a diameter of 1.35 ± 0.15 nm.

Moreover, the optical properties of CeO_2-NPs at solid-state were also investigated by recording the DRS spectrum, displayed in Fig. 3C. The measured intensity was expressed as the value of the Kubelka-Munk function F(R) (see Fig. 3C) which indicates an absorption at $\lambda < 300$ nm. The optical band gap for the transition from the valence band (V_B) to the conduction band (C_B) was calculated by linearization of the graph of $(F(R)h\nu)^{1/2}$ against photon energy (as shown in Fig. 3D) and was equal to 3.1 eV, in agreement with the literature that reports a strikingly dependence on the preparation method [46].

3.2. Photodegradation experimental results

A first experiment was conducted in the absence of the catalyst, to verify eventual photodegradation due to the UV irradiation (Fig. S.4). As revealed, a maximum conversion was observed to be 5%, reaching a stable plateau value. This concludes that ibuprofen can be considered rather stable under UV light. A second blank experiment was conducted

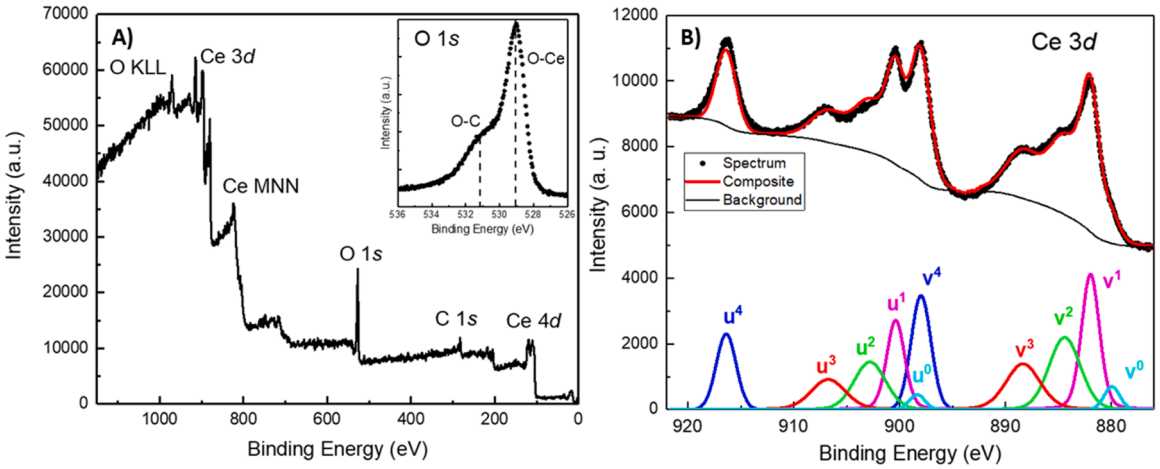

Fig. 2. **A**) XPS survey scan and O 1*s* spectrum **B**) Ce 3*d* XPS spectrum of the CeO_2 NPs.

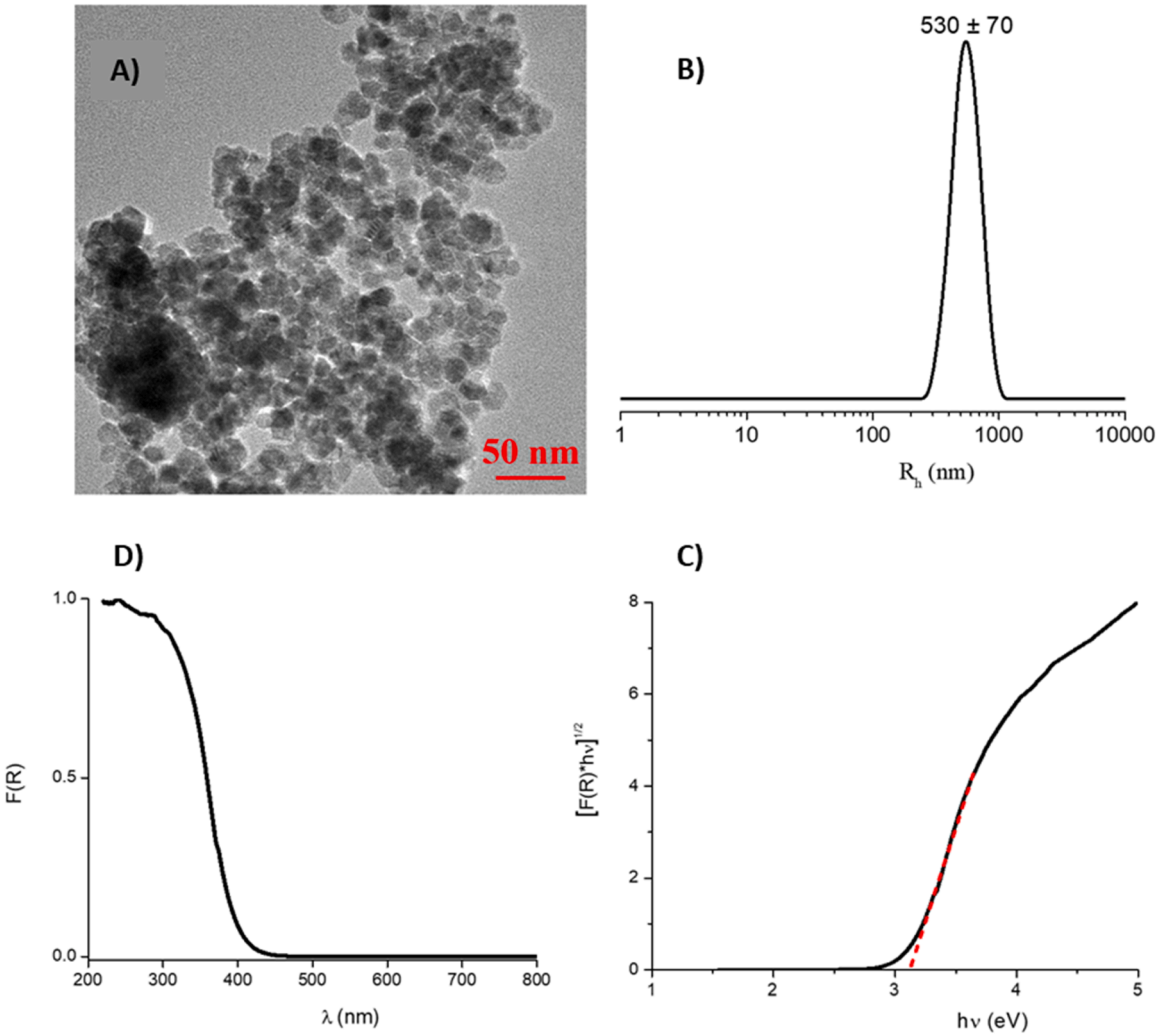

Fig. 3. **A**) TEM image, **B**) hydrodynamic radius distribution of CeO_2 NP in the aqueous medium, **C**) UV-DRS spectrum of powdered CeO_2.NPs, and **D**) estimation of the optical band gap using the modified Kubelka-Munk function.

by putting in contact the ibuprofen solution with CeO_2 nanoparticles, in the absence of UV irradiation. In this case, no ibuprofen adsorption was observed, probably due to the slightly big dimension of ibuprofen compared to the catalyst pores.

Furthermore, the synthesized material was compared with Aeroxide TiO_2-P25 which is considered nowadays a benchmark catalyst for photodegradation studies. Considering the fixed operation.

conditions, Aeroxide TiO_2-P25 shows slightly better performance

compared to CeO_2 (Fig. 4A). This promising result proves the novelty of these nanomaterials that can be attributed to their lower band-gap value (2.95 eV versus 3.30 eV of TiO_2-P25), thus, considered promising in an eventual industrial application. Before investigating the reaction kinetics, the catalyst was recovered from the experiment and reused for 5 times, to check the catalyst stability. The results are reported in Fig. 4B. In addition, TEM images for the reused CeO_2 NPs (Fig. S.5) showed no significant difference compared to Fig. 3A showing good stability as well as recyclability under the reaction conditions.

Different experiments were conducted to check the influence of both gas-liquid and liquid-solid mass transfer resistances. In particular, the airflow fed to the reactor was varied to verify whether the gas-liquid mass transfer could affect the overall rate of the reaction network (Fig. S.6). It can be concluded that by increasing the airflow, an increase in the reaction rate can be observed, reaching a stable plateau at $1.0 \cdot 10^{-6}$ m^3/s of airflow, confirming that gas-liquid mass transfer resistance can be neglected. Thus, all the other experiments were conducted imposing $1.0 \cdot 10^{-6}$ m^3/s airflow.

The impeller rate was varied in a range of 250–750 rpm to detect the optimal stirring rate to avoid fluid-solid mass transfer limitation (see Fig. S.7). It was found that beyond 500 rpm, a stable reaction rate was measured. Thus, the kinetics investigation was conducted imposing an optimal stirring rate of 750 rpm.

The influence of the reaction temperature was also investigated, as shown in Fig. 5. It is noted that by increasing the reaction temperature, an increase in the reaction conversion can be observed. When analyzing the samples, a second absorption peak was observed at $\lambda = 260$ nm, corresponding to 1-OXO ibuprofen, the most probable byproduct that can be formed [47]. This compound was verified by HPLC mass analysis. No further by-products were detected neither by HPLC mass nor by UV-Vis. It is likely that further photodegradation products will be formed at longer reaction times under harsh reaction conditions. The evolution of the by-product concentration with temperature follows a logical trend, showing an increase in the initial formation rate with temperature, passing then through a maximum as a result of its further photodegradation.

The influence of the catalyst loading on the reaction rate was investigated by conducting experiments using different bulk densities. Fig. 6 shows that by increasing the catalyst concentration, an increase in ibuprofen photodegradation was measured. Even the by-product shows a higher consumption after a higher rate of formation.

Finally, three different experiments were performed that varied the initial concentration of ibuprofen to verify the reaction order (Fig. 7). The results show that the higher the initial content of the contaminant, the faster the reaction rate, suggesting a first-order reaction. This aspect will be better described and discussed in the following experimental data kinetics modeling section. The same behavior was observed for 1-OXO ibuprofen, suggesting a higher formation rate when a more concentrated contaminant solution is used.

3.3. Kinetics modeling

To interpret the kinetics data, several assumptions must be made based on the experimental observations. First, as only ibuprofen and 1-OXO ibuprofen were detected, an in-series reaction mechanism was proposed, passing through the formation of 1-OH ibuprofen [48]. Thus, the following reaction mechanism was imposed:

$$\begin{aligned} IBU \; + \; O_2 &\xrightarrow{r_1} \; 1-OH \\ 1-OH \; + O_2 &\xrightarrow{r_2} \; 1-OXO \\ 1-\mathrm{OXO} \; + O_2 &\xrightarrow{r_3} \; other\ products \end{aligned} \tag{3}$$

Each elementary step was considered of a first-order for oxygen, taken at saturation. No adsorption was considered as the concentrations of both reactant and products are rather low. This assumption was confirmed by simple linearization, where $\ln(c_{IBu}/c_{IBu,0})$ was plotted vs. the experimental time, as demonstrated in Eq. (4).

$$\begin{aligned} \frac{dc_{IBU}}{dt} = -r\rho_B^n \rightarrow \frac{dc_{IBU}}{dt} = -kc_{IBU}\rho_B^n \rightarrow \int_{c_{IBU,0}}^{c_{IBU}} \frac{dc_{IBU}}{c_{IBU}} \\ = \int_0^t -k\rho_B^n dt \rightarrow \ln\left(\frac{c_{IBU}}{c_{IBU,0}}\right) = -k\rho_B^n t \end{aligned} \tag{4}$$

Data are aligned to a straight line, as revealed previously in Fig. 6C, demonstrating that the reaction kinetics follow a first-order rate law.

The oxygen concentration was considered to vary with temperature, imposing the following empirical equation fitted to the data published in the literature [42], to ensure the right oxygen concentration calculated at the temperature chosen for each experiment, Eq. (5).

$$c_{O_2} = \left(52.94\exp\left(-T/25.9\right) + 7.5{\cdot}10^{-4}\right)\rho_{H_2O} \tag{5}$$

The experimental data were interpreted with a pseudo-homogeneous single-phase model, since there were no fluid-solid or intraparticle diffusion limitations, from the results reported in the previous section. In particular, the Weisz-Prater criterion was calculated to ensure that intraparticle limitations were absent, but as particles were rather small (500 nm aggregates), this result suggests that no diffusion limitations affect the reaction kinetics. The general mass balance equation that was adopted is reported in Eq. (6).

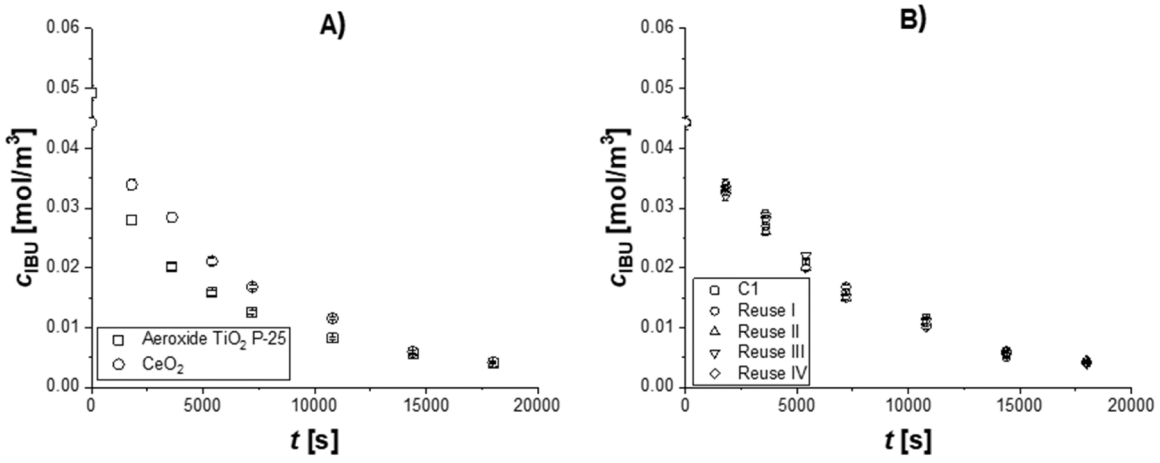

Fig. 4. (**A**) Comparison between TiO_2-P25 and CeO_2-NPs towards ibuprofen photodegradation. Adopted reaction conditions: $T = 303$ K, $c_{IBU,0} = 5 \cdot 10^{-2}$ mol/m^3, $\rho_B = 0.37$ kg/m^3, $\nu = 750$ rpm, UV irradiation. **B**) Results of reuse tests, in terms of ibuprofen concentration vs reaction time for different reuses. Experimental conditions: $T = 303$ K, $c_{IBU,0} = 5 \cdot 10^{-2}$ mol/m^3, $\rho_B = 0.37$ kg/m^3, $Q_{air} = 1.0 \cdot 10^{-6}$ m^3/s, and $\nu = 750$ rpm.

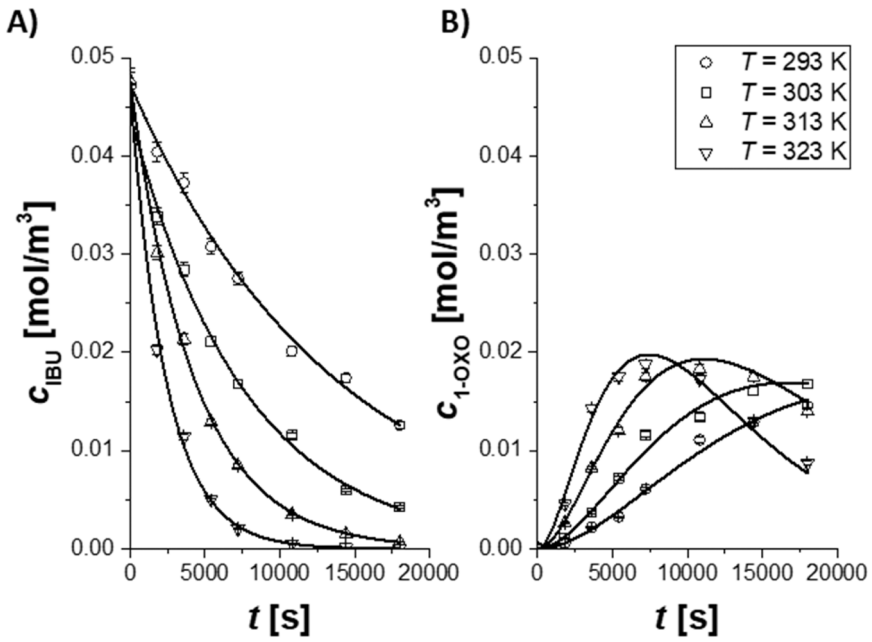

Fig. 5. Experimental results of the kinetic tests conducted at different temperatures, fixing $c_{IBU,0} = 5 \cdot 10^{-2}$ mol/m^3, $\rho_B = 0.37$ kg/m^3, $Q_{air} = 1.0 \cdot 10^{-6}$ m^3/s and $\nu = 750$ rpm. Trends of the concentration profiles vs the reaction time for **A**) ibuprofen and **B**) 1-OXO ibuprofen. Lines are the calculated profiles. The subplots refer to the same legend.

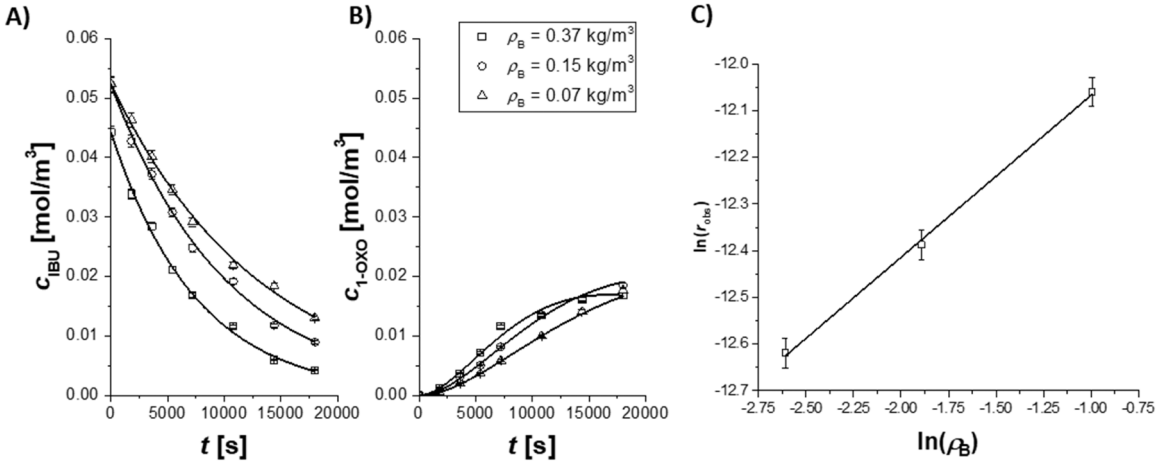

Fig. 6. Experimental results of the kinetic tests conducted at different catalyst loading, fixing $c_{IBU,0} = 5 \cdot 10^{-2}$ mol/m^3, $T = 303$ K, $Q_{air} = 1.0 \cdot 10^{-6}$ m^3/s and $\nu = 750$ rpm. Trends of the concentration profiles vs the reaction time for **A**) ibuprofen and **B**) 1-OXO ibuprofen. Lines are the calculated profiles. The subplots refer to the same legend. The panel **C**) represents catalyst bulk density linearization test.

$$\frac{dc_i}{dt} = \sum_{j=1}^{N_r} \upsilon_{ij} r_j \rho_B^n \tag{6}$$

The bulk density was elevated to a proportional coefficient n, to take into account the shielding effect of the catalyst loading on the UV-light penetration in the liquid phase [44]. This coefficient can be calculated directly from the experimental data, plotting the $\ln(r_{obs})$ vs $\ln(\rho_B)$, as in Eq. (7).

$$r_{obs} = r\rho_B^n \rightarrow \ln(r_{obs}) = \ln(r) + n\ln(\rho_B) \tag{7}$$

It is observed that the data are linear in Fig. 5C and the calculated coefficient is $n = 0.35 \pm 0.01$.

A parameter estimation analysis was performed simultaneously on C1, C6–C10 (Table S.1), to retrieve kinetic information, the kinetics constant was calculated at a reference temperature $T_{ref} = 303$ K, and activation energy for each reaction, adopting the modified Arrhenius equation reported in Eq. (8).

$$k_j = k_{ref,j} \exp\left(\frac{-Ea_j}{R}\left(\frac{1}{T} - \frac{1}{T_{ref}}\right)\right) \tag{8}$$

The summary of the obtained parameters, together with statistical information are reported in Table 2, while the obtained fits are presented earlier in Figs. 5–7.

The calculated activation energies presented in Table 2 are all within a range of kinetics regime. The three constants are of the same order of magnitude; thus, no rate-determining step can be assumed among the reactions involved. The calculated errors on all the kinetic parameters are below 12%. Only a slight correlation can be seen among the parameters. Hence, from Figs. 5–7 it is evident that the fit can be considered more than acceptable, confirming the goodness of the assumptions made.

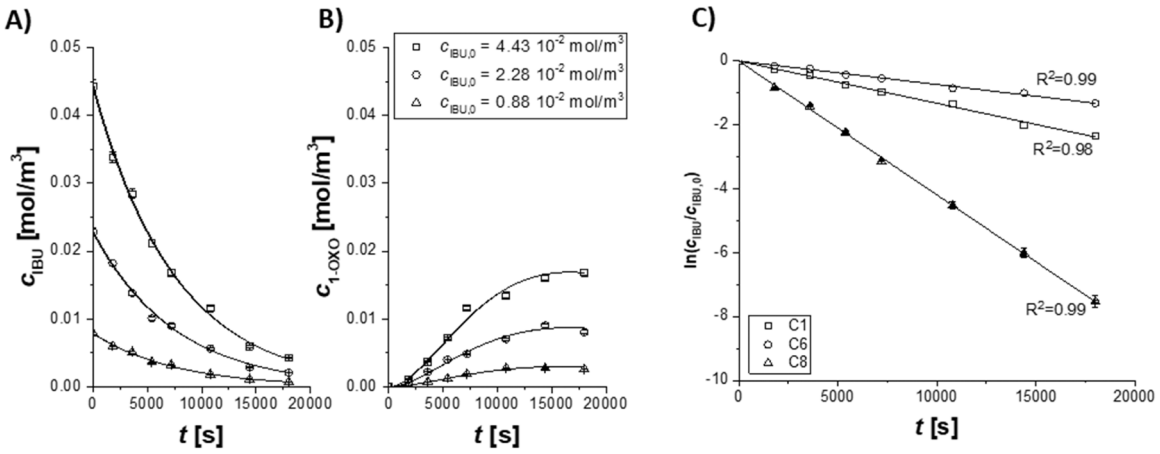

Fig. 7. Experimental results of the kinetic tests conducted at different initial concentrations of ibuprofen, fixing $T = 303$ K, $\rho_B = 0.37$ kg/m^3, $Q_{air} = 1.0 \cdot 10^{-6}$ m^3/s and $v = 750$ rpm. Trends of the concentration profiles vs the reaction time for **A**) ibuprofen and **B**) 1-OXO ibuprofen. Lines are the calculated profiles. The subplots refer to the same legend. Panel **C**) represents first-order linearization test.

Table 2
Summary of the estimated kinetic parameters, together with statistical information. $T_{ref} = 303$ K, CI 95% represents the confidence interval at 95%, *M* the correlation matrix.

Parameter	Value ± CI 95%	Units	%Error	M	$k_{ref,1}$	Ea_1	$k_{ref,2}$	Ea_2	$k_{ref,2}$	Ea_3
$k_{ref,1}$	$(1.59 \pm 0.05) \cdot 10^{-4}$	$(m^3/mol)(m^3/kg^n)s^{-1}$	1.3	$k_{ref,1}$	1.0					
Ea_1	55.8 ± 0.6	kJ/mol	1.0	Ea_1	-0.2	1.0				
$k_{ref,2}$	$(2.01 \pm 0.11) \cdot 10^{-4}$	$(m^3/mol)(m^3/kg^n)s^{-1}$	5.5	$k_{ref,2}$	-0.2	0.1	1.0			
Ea_2	29 ± 3	kJ/mol	11.8	Ea_2	0.1	-0.1	-0.6	1.0		
$k_{ref,3}$	$(1.08 \pm 0.07) \cdot 10^{-4}$	$(m^3/mol)(m^3/kg^n)s^{-1}$	6.1	$k_{ref,3}$	0.1	-0.1	0.7	-0.5	1.0	
Ea_3	31 ± 3	kJ/mol	10.6	Ea_3	-0.1	0.1	-0.6	0.5	-0.8	1.0

3.4. Thermodynamics analysis

The effect of different temperatures, i.e., 293, 303, 313, and 323 K on ibuprofen photodegradation using CeO_2-NPs was investigated. Table 3 summarizes the obtained rate constants and the corresponding values of the thermodynamic parameters namely; ΔG°, ΔH°, and ΔS°. It can be observed that increasing the reaction temperature, increases the rate constants and the corresponding photodegradation efficiency. This was previously confirmed in Fig. 5 and in the kinetics modeling section where the probability of collisions increases yielding into enhancing the photodegradation efficiency [49]. To estimate the thermodynamic parameters, Eqs. (9)–(11) were used.

$$\Delta H^\circ = E_a + RT \tag{9}$$

$$\ln(k/T) = \ln(K_B/h) + (\Delta S^\circ/R) - (\Delta H^\circ/RT) \tag{10}$$

$$\Delta G^\circ = \Delta H^\circ - T\Delta S^\circ \tag{11}$$

Where, ΔG° is the activation Gibbs free energy, ΔH° the change in enthalpy, ΔS° is the change in entropy, R is the ideal gas constant (8.314 J/mol K), K_B is Boltzmann constant (1.38×10^{-23} m^2 kg/s^2 K), h Plank constant (6.63×10^{-34} m^2 kg/s), k is the kinetics rate constant $(m^3/mol)s^{-1}$.

The relatively high positive values of ΔG° and ΔH° designate the endothermic non-spontaneous reaction forming a highly hydrated transition state complex with weak bonds for rapid degradation of the activated complex [49–51]. Moreover, the negative value of ΔS°, which is close to zero, suggests that the system exhibits a random behavior that supports a higher degree of degradation of ibuprofen into simple products [49].

4. Conclusions

This work investigates the ability of CeO_2 nanostructured materials, obtained by the wet-chemical approach, to exert a notable photodegradation of ibuprofen. The synthesis strategy led to the successful preparation of small crystalline CeO_2-NPs with a size of about 15 nm and a band gap of 3.1 eV against which the synthesized material showed comparable photocatalytic activity. XPS analysis was performed to gain a deeper understanding of the chemical composition of the surface of the CeO_2-NPs, where the ratio of Ce^{3+}/Ce^{4+} was estimated to be 0.4, as deduced from the areas of these different components. Based on the air flow rate and stirring speed study, both fluid-solid and intraparticle diffusion limitations can be neglected. The reusability of the CeO_2-NPs study indicated that they can be used repeatedly, without impacting their capacity, confirming their sustainability. It is worth mentioning, that CeO_2-NPs show similar activity to the commercial TiO_2-P25, hence the use of Ce can be more convenient when considering its market price

Table 3
Kinetic and thermodynamic parameters for the photodegradation of ibuprofen using CeO_2-NPs at $E_{a1} = 55.8 kJ/mol$.

T (K)	K $(m^3/mol)s^{-1}$	$\ln(k/T)$	$\Delta H^\circ/RT$	ΔH° $(kJ\,mol^{-1})$	ΔS° $(kJ\,mol^{-1}\,K^{-1})$	ΔG° $(kJ\,mol^{-1})$
293	2.7×10^{-5}	-16.18	23.91	58.2	− 0.14	100.0
303	5.9×10^{-5}	-15.45	23.15	58.3		101.5
313	1.2×10^{-4}	-14.78	22.44	58.4		103.0
323	2.3×10^{-4}	-14.15	21.78	58.5		104.5

that is lower than Ti. For the kinetics modeling, the experimental data were interpreted with a pseudo homogeneous single-phase model. The calculated activation energies were all within a range of the kinetic regime, with no rate-determining step among the involved reactions. The thermodynamic parameters of the photodegradation of ibuprofen have been reported. The relatively high positive values of ΔG° and ΔH° indicate the endothermic and nonspontaneous nature of the reaction forming a highly hydrated transition state complex with weak bonds for rapid degradation of the activated complex. While the positive value of ΔS° suggests that the system exhibits a random behavior with enhanced photodegradation performance of CeO_2 NPs towards ibuprofen. Overall, the findings promote the use of such a promising CeO_2 nanostructure for industrial level for ibuprofen-based pharmaceutical wastewater treatment.

CRediT authorship contribution statement

Vincenzo Russo and Giuseppe Vitiello wrote the original draft of the manuscript. The main conceptual ideas were drawn from the interactions between Vincenzo Russo and Giuseppe Vitiello, while the funds were obtained by the synergistic effect of the cooperation between Martino Di Serio and Luigi Paduano. The experimental work, data elaboration, and the formal analysis were carried out by Noemi Gallucci, Maryam Hmoudah, Amjad El-Qanni, and Eugenie Martinez. The final draft was revised by Giuseppe Vitiello and Vincenzo Russo.

Funding

The 12th executive program for scientific and technological cooperation between the Italian Republic and the Republic of Korea for the years 2019–2021 is acknowledged for financial support.

This project has received funding from the EU-H2020 Research and Innovation Program under Grant agreement no. 2018.1:677 (ID677), having benefitted from the access provided by CEA-LETI in Grenoble (France) within the framework of the NFFA-Europe Transnational Access Activity.

Declaration of Competing Interest

The authors declare that they have no known competing financial interests or personal relationships that could have appeared to influence the work reported in this paper.

Acknowledgments

The authors are grateful to Dr. Rocco Di Girolamo (Department of Chemical Science, University of Naples Federico II) for his support in TEM analysis and to Marica Chianese for her experimental support in conducting the kinetic experiments. The authors also thank CEA-LETI (Grenoble, France) for providing the access to XPS instrument.

Appendix A. Supporting information

Supplementary data associated with this article can be found in the online version at doi:10.1016/j.jece.2022.107866.

References

[1] B. Xu, F. Qi, D. Sun, Z. Chen, D. Robert, Cerium doped red mud catalytic ozonation for bezafibrate degradation in wastewater: efficiency, intermediates, and toxicity, Chemosphere 146 (2016) 22–31, https://doi.org/10.1016/j.chemosphere.2015.12.016.

[2] A. Kumar, G. Sharma, M. Naushad, A.a.H. Al-Muhtaseb, A. Kumar, I. Hira, T. Ahamad, A.A. Ghfar, F.J. Stadler, Visible photodegradation of ibuprofen and 2,4-D in simulated waste water using sustainable metal free-hybrids based on carbon nitride and biochar, J. Environ. Manag., vol. 231, 2019, pp. 1164–75. (https://doi.org/10.1016/j.jenvman.2018.11.015).

[3] S. Saeid, P. Tolvanen, N. Kumar, K. Eränen, J. Peltonen, M. Peurla, J.-P. Mikkola, A. Franz, T. Salmi, Advanced oxidation process for the removal of ibuprofen from aqueous solution: a non-catalytic and catalytic ozonation study in a semi-batch reactor, Appl. Catal. B: Environ. 230 (2018) 77–90, https://doi.org/10.1016/j.apcatb.2018.02.021.

[4] S.D. Richardson, S.Y. Kimura, Water analysis: emerging contaminants and current issues, Anal. Chem. 92 (1) (2020) 473–505, https://doi.org/10.1021/acs.analchem.9b05269.

[5] L.F.V. Francisco, B. do Amaral Crispim, J.C.V. Spósito, J.C.J. Solórzano, N. H. Maran, F. Kummrow, V.A. do Nascimento, C.C. Montagner, K.M.P. De Oliveira, A. Barufatti, Metals and emerging contaminants in groundwater and human health risk assessment, Environ. Sci. Pollut. Res. 26 (24) (2019) 24581–24594, https://doi.org/10.1007/s11356-019-05662-5.

[6] B.S. Rathi, P.S. Kumar, P.-L. Show, A review on effective removal of emerging contaminants from aquatic systems: current trends and scope for further research, J. Hazard. Mater. (2020), 124413, https://doi.org/10.1016/j.jhazmat.2020.124413.

[7] P.R. Rout, T.C. Zhang, P. Bhunia, R.Y. Surampalli, Treatment technologies for emerging contaminants in wastewater treatment plants: a review, Sci. Total Environ. 753 (2021), 141990, https://doi.org/10.1016/j.scitotenv.2020.141990.

[8] H. Chaker, S. Fourmentin, L. Chérif-Aouali, Efficient photocatalytic degradation of ibuprofen under visible light irradiation using silver and cerium Co-doped mesoporous TiO_2, ChemistrySelect 5 (38) (2020) 11787–11796, https://doi.org/10.1002/slct.202002730.

[9] G. Boczkaj, A. Fernandes, Wastewater treatment by means of advanced oxidation processes at basic pH conditions: a review, Chem. Eng. J. 320 (2017) 608–633, https://doi.org/10.1016/j.cej.2017.03.084.

[10] A. Gul, N.G. Khaligh, N.M. Julkapli, Surface modification of carbon-based nanoadsorbents for the advanced wastewater treatment, J. Mol. Struct. 1235 (2021), 130148, https://doi.org/10.1016/j.molstruc.2021.130148.

[11] A. El-Qanni, Development of Sustainable Nanosorbcats Based Technology for Hydrocarbons and Organic Pollutants Recovery from Industrial Wastewater, Chemical and Petroleum Engineering, University of Calgary, Calgary, AB, 2017.

[12] A. Ahmad, S.H. Mohd-Setapar, C.S. Chuong, A. Khatoon, W.A. Wani, R. Kumar, M. Rafatullah, Recent advances in new generation dye removal technologies: novel search for approaches to reprocess wastewater, RSC Adv. 5 (39) (2015) 30801–30818, https://doi.org/10.1039/C4RA16959J.

[13] I. Gehrke, A. Geiser, A. Somborn-Schulz, Innovations in nanotechnology for water treatment, Nanotechnol. Sci. Appl. 8 (2015) 1–17, https://doi.org/10.2147/NSA.S43773.

[14] A.S. Adeleye, J.R. Conway, K. Garner, Y. Huang, Y. Su, A.A. Keller, Engineered nanomaterials for water treatment and remediation: costs, benefits, and applicability, Chem. Eng. J. 286 (2016) 640–662, https://doi.org/10.1016/j.cej.2015.10.105.

[15] S. Dong, J. Feng, M. Fan, Y. Pi, L. Hu, X. Han, M. Liu, J. Sun, J. Sun, Recent developments in heterogeneous photocatalytic water treatment using visible light-responsive photocatalysts: a review, RSC Adv. 5 (19) (2015) 14610–14630, https://doi.org/10.1039/C4RA13734E.

[16] M.A. Sousa, C. Gonçalves, V.J.P. Vilar, R.A.R. Boaventura, M.F. Alpendurada, Suspended TiO_2-assisted photocatalytic degradation of emerging contaminants in a municipal WWTP effluent using a solar pilot plant with CPCs, Chem. Eng. J. 198–199 (2012) 301–309, https://doi.org/10.1016/j.cej.2012.05.060.

[17] C. Tortajada, Contributions of recycled wastewater to clean water and sanitation sustainable development goals, npj Clean Water 3 (1) (2020) 22, https://doi.org/10.1038/s41545-020-0069-3.

[18] M. Vatanparast, L. Saedi, Sonochemical-assisted synthesis and characterization of CeO_2 nanoparticles and its photocatalytic properties, J. Mater. Sci.: Mater. Electron. 29 (9) (2018) 7107–7113, https://doi.org/10.1007/s10854-018-8698-8.

[19] S. Yuán, B. Xu, Q. Zhang, S. Liu, J. Xie, M. Zhang, T. Ohno, Development of the visible-light response of CeO_{2-x} with a high Ce^{3+} content and its photocatalytic properties, ChemCatChem 10 (6) (2018) 1267–1271, https://doi.org/10.1002/cctc.201701767.

[20] L. Gnanasekaran, R. Hemamalini, R. Saravanan, K. Ravichandran, F. Gracia, S. Agarwal, V.K. Gupta, Synthesis and characterization of metal oxides (CeO_2, CuO, NiO, Mn_3O_4, SnO_2 and ZnO) nanoparticles as photo catalysts for degradation of textile dyes, J. Photochem. Photobiol. B: Biol. 173 (2017) 43–49, https://doi.org/10.1016/j.jphotobiol.2017.05.027.

[21] M. Aslam, M.T. Qamar, M.T. Soomro, I.M.I. Ismail, N. Salah, T. Almeelbi, M. A. Gondal, A. Hameed, The effect of sunlight induced surface defects on the photocatalytic activity of nanosized CeO_2 for the degradation of phenol and its derivatives, Appl. Catal. B: Environ. 180 (2016) 391–402, https://doi.org/10.1016/j.apcatb.2015.06.050.

[22] P. Borker, A.V. Salker, Solar assisted photocatalytic degradation of naphthol blue black dye using $Ce_{1-x}Mn_xO_2$, Mater. Chem. Phys. 103 (2) (2007) 366–370, https://doi.org/10.1016/j.matchemphys.2007.02.034.

[23] D. Majumder, I. Chakraborty, K. Mandal, S. Roy, Facet-dependent photodegradation of methylene blue using pristine CeO_2 nanostructures, ACS Omega 4 (2) (2019) 4243–4251, https://doi.org/10.1021/acsomega.8b03298.

[24] F. Naaz, U. Farooq, T. Ahmad, Ceria as an efficient nanocatalyst for organic transformations, nanocatalysts, IntechOpen (2019), https://doi.org/10.5772/intechopen.82688.

[25] J.A. Rodriguez, D.C. Grinter, Z. Liu, R.M. Palomino, S.D. Senanayake, Ceria-based model catalysts: fundamental studies on the importance of the metal–ceria interface in CO oxidation, the water–gas shift, CO_2 hydrogenation, and methane and alcohol reforming, Chem. Soc. Rev. 46 (7) (2017) 1824–1841, https://doi.org/10.1039/C6CS00863A.

[26] C. Maria Magdalane, K. Kaviyarasu, A. Raja, M.V. Arularasu, G.T. Mola, A.B. Isaev, N.A. Al-Dhabi, M.V. Arasu, B. Jeyaraj, J. Kennedy, M. Maaza, Photocatalytic decomposition effect of erbium doped cerium oxide nanostructures driven by visible light irradiation: investigation of cytotoxicity, antibacterial growth inhibition using catalyst, J. Photochem. Photobiol. B: Biol. 185 (2018) 275–282, https://doi.org/10.1016/j.jphotobiol.2018.06.011.
[27] S.M.M. (SMM), SMM Spot prices. ⟨https://www.metal.com/⟩, (Accessed 3rd June 2021).
[28] A.S. Weber, A.M. Grady, R.T. Koodali, Lanthanide modified semiconductor photocatalysts, Catal. Sci. Technol. 2 (4) (2012) 683–693, https://doi.org/10.1039/C2CY00552B.
[29] M.E. Kibar, Preparation of copper oxide-cerium oxide/nanotube-titanium dioxide photocatalyst for CO_2 conversion in solar light, React. Kinet. Mech. Catal. 134 (2) (2021) 937–950, https://doi.org/10.1007/s11144-021-02079-5.
[30] M. Ahamed, M.A.M. Khan, M.J. Akhtar, H.A. Alhadlaq, A. Alshamsan, Ag-doping regulates the cytotoxicity of TiO_2 nanoparticles via oxidative stress in human cancer cells, Sci. Rep. 7 (1) (2017) 17662, https://doi.org/10.1038/s41598-017-17559-9.
[31] Y.-C. Zhang, Z. Li, L. Zhang, L. Pan, X. Zhang, L. Wang, A. Fazal e, J.-J. Zou, Role of oxygen vacancies in photocatalytic water oxidation on ceria oxide: experiment and DFT studies, Appl. Catal. B: Environ. 224 (2018) 101–108, https://doi.org/10.1016/j.apcatb.2017.10.049.
[32] M. Ahamed, M.J. Akhtar, M.A.M. Khan, Z.M. Alaizeri, H.A. Alhadlaq, Evaluation of the cytotoxicity and oxidative stress response of CeO_2-RGO nanocomposites in human lung epithelial A549 cells, Nanomaterials 9 (12) (2019) 1709.
[33] M.M. Khan, S.A. Ansari, D. Pradhan, D.H. Han, J. Lee, M.H. Cho, Defect-induced band gap narrowed CeO_2 nanostructures for visible light activities, Ind. Eng. Chem. Res. 53 (23) (2014) 9754–9763, https://doi.org/10.1021/ie500986n.
[34] G. Jayakumar, A. Albert Irudayaraj, A. Dhayal Raj, Particle size effect on the properties of cerium oxide (CeO_2) nanoparticles synthesized by hydrothermal method, mechanics, Mater. Sci. Eng. J. 9 (1) (2017), https://doi.org/10.2412/mmse.3.4.481.
[35] B. Choudhury, A. Choudhury, Ce^{3+} and oxygen vacancy mediated tuning of structural and optical properties of CeO_2 nanoparticles, Mater. Chem. Phys. 131 (3) (2012) 666–671, https://doi.org/10.1016/j.matchemphys.2011.10.032.
[36] C. Yang, X. Yu, P.N. Pleßow, S. Heißler, P.G. Weidler, A. Nefedov, F. Studt, Y. Wang, C. Wöll, Rendering photoreactivity to ceria: the role of defects, Angew. Chem. Int. Ed. 56 (45) (2017) 14301–14305, https://doi.org/10.1002/anie.201707965.
[37] J.K. Sharma, P. Srivastava, S. Ameen, M.S. Akhtar, S.K. Sengupta, G. Singh, Phytoconstituents assisted green synthesis of cerium oxide nanoparticles for thermal decomposition and dye remediation, Mater. Res. Bull. 91 (2017) 98–107, https://doi.org/10.1016/j.materresbull.2017.03.034.
[38] P. Latha, K. Prakash, S. Karuthapandian, Effective photodegradation of CR & MO dyes by morphologically controlled cerium oxide nanocubes under visible light illumination, Optik 154 (2018) 242–250, https://doi.org/10.1016/j.ijleo.2017.10.054.
[39] S. Sehar, I. Naz, A. Rehman, W. Sun, S.S. Alhewairini, M.N. Zahid, A. Younis, Shape-controlled synthesis of cerium oxide nanoparticles for efficient dye photodegradation and antibacterial activities, Appl. Organomet. Chem. 35 (1) (2021), e6069, https://doi.org/10.1002/aoc.6069.
[40] S.J. Saadoon, M. Jarosova, P. Machek, M.M. Kadhim, M.H. Ali, A.D. Khalaji, Methylene blue photodegradation using as-synthesized CeO_2 nanoparticles, J. Chin. Chem. Soc. n/a (n/a) (2021), https://doi.org/10.1002/jccs.202100476.
[41] N.M. Lopés-Velasco, S.J. Bailón-Ruiz, Effect of the particle size and pH on the photocatalytic performance of cerium oxide (CeO_2) nanoparticles, MRS Adv. 6 (32) (2021) 769–773, https://doi.org/10.1557/s43580-021-00070-9.
[42] A.I.Y. Tok, F.Y.C. Boey, Z. Dong, X.L. Sun, Hydrothermal synthesis of CeO_2 nanoparticles, J. Mater. Process. Technol. 190 (1) (2007) 217–222, https://doi.org/10.1016/j.jmatprotec.2007.02.042.
[43] E.P. Barrett, L.G. Joyner, P.P. Halenda, The determination of pore volume and area distributions in porous substances. I. Computations from nitrogen isotherms, J. Am. Chem. Soc. 73 (1) (1951) 373–380, https://doi.org/10.1021/ja01145a126.
[44] D. Girija, H.S.B. Naik, C. Sudhamani, B.V. Kumar, Cerium oxide nanoparticles—a green, reusable, and highly efficient heterogeneous catalyst for the synthesis of polyhydroquinolines under solvent-free conditions, Arch. Appl. Sci. Res. 3 (3) (2011) 373–382.
[45] M. Okuda, Y. Suzumoto, I. Yamashita, Bioinspired synthesis of homogenous cerium oxide nanoparticles and two- or three-dimensional nanoparticle arrays using protein supramolecules, Cryst. Growth Des. 11 (6) (2011) 2540–2545, https://doi.org/10.1021/cg200299y.
[46] E. Kusmierek, A CeO_2 semiconductor as a photocatalytic and photoelectrocatalytic material for the remediation of pollutants in industrial wastewater: a review, Catalysts 10 (12) (2020), https://doi.org/10.3390/catal10121435.
[47] M. Kråkström, S. Saeid, P. Tolvanen, N. Kumar, T. Salmi, L. Kronberg, P. Eklund, Identification and quantification of transformation products formed during the ozonation of the non-steroidal anti-inflammatory pharmaceuticals ibuprofen and diclofenac, Ozone: Sci. Eng. (2021) 1–15, https://doi.org/10.1080/01919512.2021.1898928.
[48] S. Saeid, M. Kråkström, P. Tolvanen, N. Kumar, K. Eränen, M. Peurla, J.-P. Mikkola, L. Maël, L. Kronberg, P. Eklund, T. Salmi, Synthesis and characterization of metal modified catalysts for decomposition of ibuprofen from aqueous solutions, Catalysts 10 (7) (2020), https://doi.org/10.3390/catal10070786.
[49] K. Byrappa, A.K. Subramani, S. Ananda, K.M.L. Rai, R. Dinesh, M. Yoshimura, Photocatalytic degradation of rhodamine B dye using hydrothermally synthesized ZnO, Bull. Mater. Sci. 29 (5) (2006) 433–438, https://doi.org/10.1007/BF02914073.
[50] M. Rezaei, A. Nezamzadeh-Ejhieha, The ZnO-NiO nano-composite: a brief characterization, kinetic and thermodynamic study and study the Arrhenius model on the sulfasalazine photodegradation, Int. J. Hydrog. Energy 45 (46) (2020) 24749–24764, https://doi.org/10.1016/j.ijhydene.2020.06.258.
[51] A.S.M. Kuba, A.M.J.A.L. Shamari, Kinetics and thermodynamics study for photodegradation of brown HT dye by MnO and NiO as catalysis, Mater. Today: Proc. 49 (2022) 2741–2746, https://doi.org/10.1016/j.matpr.2021.09.256.